

Article

# Facile Synthesis of Multi-Channel Surface-Modified Amorphous Iron Oxide Nanospheres as High-Performance Anode Materials for Lithium-Ion Batteries

Shijin Yu <sup>\*</sup>, Wenzhen Zhu, Ying Wei, Jiahao Tong, Quanya Wei, Tianrui Chen, Xuannan He, Dingwen Hu, Cuiyun Li and Hua Zhu <sup>\*</sup>

School of Mechanical and Electrical Engineering, Jingdezhen Ceramic University, Jingdezhen 333001, China

<sup>\*</sup> Correspondence: yushijin@163.com (S.Y.); zwchua@163.com (H.Z.)

**Abstract:** Based on the synergistic effect of ripening and hydrogen ion etching in a hydrothermal solution, a simple, facile, and low-cost new strategy was demonstrated to prepare multi-channel surface-modified amorphous Fe<sub>2</sub>O<sub>3</sub> nanospheres as anodes for Li-ion batteries in this study. Compared with polycrystalline Fe<sub>2</sub>O<sub>3</sub>, the conversion reaction between amorphous Fe<sub>2</sub>O<sub>3</sub> and lithium ions has a lower Gibbs free energy change and a stronger reversibility, which can contribute to an elevation in the cycle capability of the electrode. Meanwhile, there are abundant active sites and more effective dangling bonds/defects in amorphous materials, which is beneficial to promote charge transfer and lithium-ion migration kinetics. The Galvanostatic intermittent titration analysis results confirmed that the amorphous Fe<sub>2</sub>O<sub>3</sub> electrode had a higher Li<sup>+</sup> diffusion coefficient. In addition, the surfaces of the amorphous nanospheres are corroded to produce multiple criss-cross channels. The multi-channel surface structure can not only increase the contact area between Fe<sub>2</sub>O<sub>3</sub> nanospheres and electrolyte, but also reserve space for volume expansion, thereby effectively alleviating the volume change during the intercalation-deintercalation of lithium ions. The electrochemical performance showed that the multi-channel surface-modified amorphous Fe<sub>2</sub>O<sub>3</sub> electrode exhibited a higher specific capacity, a more stable cycle performance, and a narrower voltage hysteresis. It is believed that amorphous metal oxides have great potential as high-performance anodes of next-generation lithium-ion batteries.

**Keywords:** lithium-ion battery; Fe<sub>2</sub>O<sub>3</sub>; amorphous; anode; electrochemical performance



**Citation:** Yu, S.; Zhu, W.; Wei, Y.; Tong, J.; Wei, Q.; Chen, T.; He, X.; Hu, D.; Li, C.; Zhu, H. Facile Synthesis of Multi-Channel Surface-Modified Amorphous Iron Oxide Nanospheres as High-Performance Anode Materials for Lithium-Ion Batteries. *Energies* **2022**, *15*, 5974. <https://doi.org/10.3390/en15165974>

Academic Editor: Christian Julien

Received: 19 July 2022

Accepted: 14 August 2022

Published: 18 August 2022

**Publisher's Note:** MDPI stays neutral with regard to jurisdictional claims in published maps and institutional affiliations.



**Copyright:** © 2022 by the authors. Licensee MDPI, Basel, Switzerland. This article is an open access article distributed under the terms and conditions of the Creative Commons Attribution (CC BY) license (<https://creativecommons.org/licenses/by/4.0/>).

## 1. Introduction

Due to their high energy/power densities and long cycle life, lithium-ion batteries (LIBs) have been widely used in portable electronic devices and electric vehicles (EV) [1]. However, the commercial graphite electrodes with a low theoretical specific capacity of 372 mAh/g cannot meet the requirements of high energy density [2,3]. Therefore, various anode materials with a higher specific capacity than graphite have been explored, such as metal [4], silicon-based materials [5,6], MXene [7], nitrides [8,9], sulfides [10], and transition metal oxides (TMOs) [11]. Iron oxide (Fe<sub>2</sub>O<sub>3</sub>) has received widespread attention due to its natural abundance, low price, non-toxicity, and high theoretical specific capacity (1007 mAh/g) [12,13]. Unfortunately, similar to other TMOs, Fe<sub>2</sub>O<sub>3</sub> also has poor electronic conductivity, high potential hysteresis, and large volume change during the charge/discharge process, leading to a rapid fading in capacity [14,15].

In contrast to the intercalation reaction of graphite electrodes, TMOs can interact with lithium through the phase conversion reaction ( $MO_x + 2xLi \leftrightarrow M + xLi_2O$ ). Therefore, the feasibility and reversibility of the reaction process are dependent on the thermodynamic and kinetic parameters of the conversion reaction. The Gibbs free energy change of the reaction between amorphous Fe<sub>2</sub>O<sub>3</sub> and lithium is 0.27 eV lower than that of its crystalline counterpart. The lower the Gibbs free energy change, the stronger the reversibility of

the conversion reaction [16,17]. Shi and Zhu combined amorphous  $\text{Fe}_2\text{O}_3$  with graphene or nitrogen-doped carbon, respectively, and the corresponding electrodes were used in lithium-ion batteries or sodium-ion batteries to achieve a high cycle stability [18,19]. Due to its isotropic properties, the amorphous material expands/shrinks uniformly in all directions during the intercalation/deintercalation of lithium ions, so it has a higher strain capacity [20–22]. It has been confirmed that anodes based on amorphous phases of Si,  $\text{Fe}_2\text{O}_3$ ,  $\text{TiO}_2$  and  $\text{SnO}_2$  could buffer the volume change and hence exhibited an improved cycle performance [23–27]. Therefore, it is expected that amorphous materials will be promising candidates as electrodes, due to their fast reaction kinetics, strong reversibility and narrow potential hysteresis [28,29].

In order to improve the electrochemical performance of the  $\text{Fe}_2\text{O}_3$  anode, various strategies have recently been proposed. For instance,  $\text{Fe}_2\text{O}_3$  has been compounded with carbonaceous materials to improve the diffusion rate of lithium ions and the conductivity of the electrode [30]. Yu et al. reported  $\text{Fe}_2\text{O}_3$ /graphene hybrid-based electrodes with largely enhanced conductivity, and a high reversible specific capacity of 658.5 mA h/g was achieved after 200 cycles at 1 A/g [31]. Another strategy is to synthesize nanostructures, such as nanowires [32], nanorods [33], nanotubes [34], nanoplates [35], nanoboxes [36], flower-like [37] and nanospheres [38]. The flower-like structure with a high surface area and abundant internal space can ensure close contact between the active material and the electrolyte and inhibit the volume change of  $\text{Li}^+$  insertion/extraction. Han et al. prepared flower-shaped hematite ( $\alpha\text{-Fe}_2\text{O}_3$ ) in a hot solution, which exhibited excellent electrochemical performance as a LIBs anode [39]. Ma et al. synthesized flower-like  $\text{Fe}_2\text{O}_3$  by thermally decomposing the reaction precursor of iron acetylacetonate and ethylene glycol, and the reversible specific capacity exceeded 800 mAh/g after 40 cycles [40].

Inspired by the above statement, we attempted to design and develop a new type of  $\text{Fe}_2\text{O}_3$  nanosphere electrode, which can provide high conductivity, high specific surface area and abundant internal space. The nanospheres were composed of amorphous  $\text{Fe}_2\text{O}_3$  particles. There are a large number of active sites and more effective dangling bonds/defects in amorphous materials, which are beneficial to promote charge transfer and lithium-ion migration kinetics, and further contributes to an elevation in rate capacity [3,41]. With its lower Gibbs free energy change and stronger reversibility, the amorphous electrode can also achieve high cycling capacity and stable cycling stability. Similar to the flower-like structure, a large number of connected channels are corroded on the surface of  $\text{Fe}_2\text{O}_3$  nanospheres to relieve the stress of volume deformation before and after lithium insertion. By a facile and low-cost route of hydrothermal method treatment, a multi-channel surface modified amorphous  $\text{Fe}_2\text{O}_3$  nanospheres electrode was fabricated in this study. Compared with its crystal counterpart, the multi-channel surface-modified amorphous  $\text{Fe}_2\text{O}_3$  electrode had a higher specific capacity, a more stable cycle performance, and a narrower voltage hysteresis.

## 2. Materials and Methods

Multi-channel surface-modified amorphous  $\text{Fe}_2\text{O}_3$  nanospheres were prepared by using a simple and low-cost hydrothermal method. A total of 0.326 g  $\text{K}_3[\text{Fe}(\text{CN})_6]$  and 0.043 g  $\text{NH}_4\text{H}_2\text{PO}_4$  were dissolved in deionized water to form a clear solution after stirring at room temperature for 30 min. Then, the solution was transferred to a hydrothermal kettle for hydrothermal treatment at 200 °C for different times (1 h, 3 h and 6 h), with the corresponding samples denoted as A1h, A3h, and A6h, respectively. The products were centrifuged and washed for three times with both deionized water and ethanol. Multi-channel surface-modified amorphous  $\text{Fe}_2\text{O}_3$  nanospheres were obtained after drying in an oven at 110 °C for 12 h. Similarly, polycrystalline  $\text{Fe}_2\text{O}_3$  nanospheres were prepared by the hydrothermal treatment of  $\text{FeCl}_3$  and  $\text{Ni}(\text{CH}_3\text{COO})_2$  precursor solutions for 1 h as a comparative sample (C1h).

Crystallinity of the as-prepared samples was characterized by using X-ray diffraction (XRD) with a Bruker-D8 X-ray diffractometer with nickel filtered copper K radiation ( $\lambda = 1.5406 \text{ \AA}$ ). Morphologies of the samples were observed by using field emission scanning

electron microscopy (FESEM, JEOL JSM-7500F) and transmission electron microscopy (TEM, JEM-2100P). Elemental compositions and chemical states were analyzed by using X-ray photoelectron spectroscopy (XPS, Thermo K-Alpha). Specific surface area of the samples was measured by using the Brunauer-Emmett-Teller (BET) method with a Micrometrics ASAP 2420 surface analyzer.

Electrochemical measurements were performed using half-coin cells. The active materials (80 wt.%) were mixed with conductive carbon black (10 wt.%) and sodium carboxymethyl cellulose (CMC, 10 wt.%) in deionized water to form slurries. The slurries were coated on nickel foam (99.5%, Alfa Aesar) as a current collector, followed by drying in a vacuum oven at 80 °C for 12 h to obtain electrodes. Coin cells (CR 2032) with lithium foil as the counter electrode were assembled in a glove box filled with high-purity Ar gas (>99.999%). An electrolyte consisting of 1 M LiPF<sub>6</sub> in a mixture of vinyl acetate (EC), ethylene carbonate (DEC), and dimethyl carbonate (DMC) (1:1:1 by volume) was used with a micro-porous polymer membrane separator (Celgard 2400). The cells were charged and discharged between 0.005 V and 3 V (versus Li/Li<sup>+</sup>) using blue electric test system (CT2001A). Galvanostatic intermittent titration technique (GITT) was employed by charging/discharging the cells at a current of 100 mA/g for 20 min and it took about 4 h until the cut-off voltage limits were reached. Prior to post-cycling characterization, the cells were charged at 3 V for 48 h to ensure the full extraction of Li. The CHI660E electrochemical analyzer was used to record cyclic voltammetry (CV) and electrochemical impedance spectroscopy (EIS). The voltage range of CV measurement was 0.01–3 V and the scan rate was 0.1 mV/s. The EIS measurement was conducted from 100 kHz to 10 MHz.

### 3. Results and Discussion

Figure 1 shows schematic diagrams describing the formation process of the multi-channel surface-modified amorphous Fe<sub>2</sub>O<sub>3</sub> nanospheres during the hydrothermal treatment and the lattice evolution of Fe<sub>2</sub>O<sub>3</sub> due to corrosion. Figure 2 shows the XRD patterns of the samples A1h and C1h. The diffraction peaks of C1h are consistent with those of α-Fe<sub>2</sub>O<sub>3</sub> (No.33-0664), indicating that it was crystalline α-Fe<sub>2</sub>O<sub>3</sub>. In contrast, A1h had no obvious diffraction peaks, suggesting that it was amorphous. As the hydrothermal treatment time was extended from 1 h to 6 h, the XRD pattern of the samples remained unchanged (Figure S1).

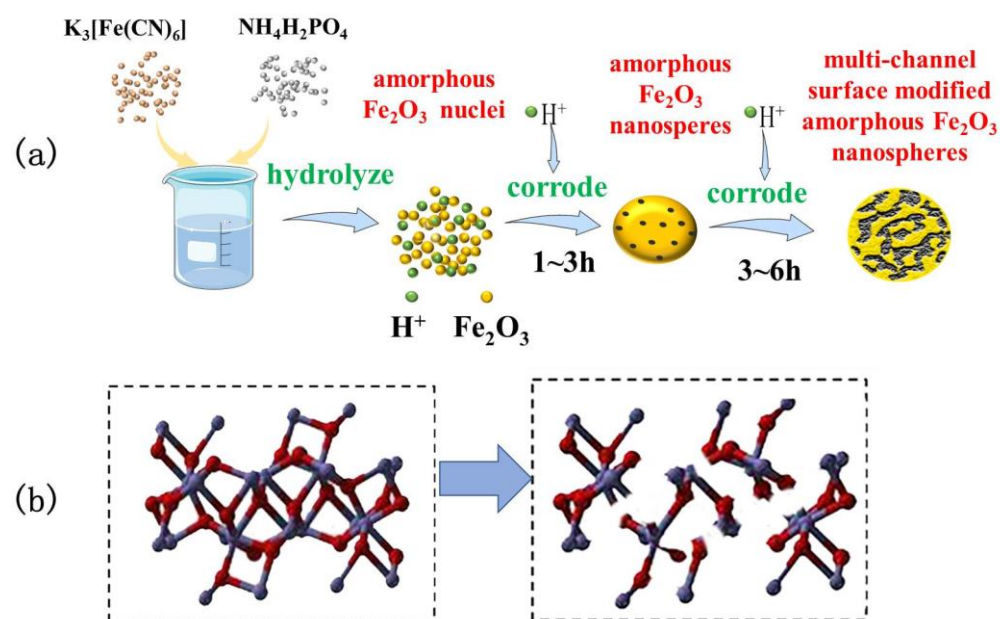


**Figure 1.** (a) Schematic diagram of the formation of the multi-channel surface-modified amorphous Fe<sub>2</sub>O<sub>3</sub> nanospheres during the hydrothermal reaction process. (b) Schematic diagram of the evolution of Fe<sub>2</sub>O<sub>3</sub> lattice due to corrosion.

Figure 3 shows the wide-scan XPS spectrum of A1h, confirming the presence of Fe and O in the amorphous sample. Fe 2p XPS spectrum is shown as an inset in Figure 3. The two peaks at 710.7 eV and 724.5 eV correspond to the binding energies of Fe 2p 3/2 and Fe 2p 1/2, respectively. The two peaks are consistent with the peaks of Fe<sup>3+</sup> [42–45]. In addition, the satellite peak at 719 eV further confirms that the cation was Fe<sup>3+</sup> [16]. Meanwhile, there is an obvious characteristic peak of lattice oxygen (O 1s) at 530 eV, as shown in Figure S2 [46,47]. Based on the XRD pattern in Figure 2, it is concluded that amorphous Fe<sub>2</sub>O<sub>3</sub> was formed in the samples (A1h) prepared by using the hydrothermal reaction method with the precursor solution of K<sub>3</sub>[Fe(CN)<sub>6</sub>] and NH<sub>4</sub>H<sub>2</sub>PO<sub>4</sub>.

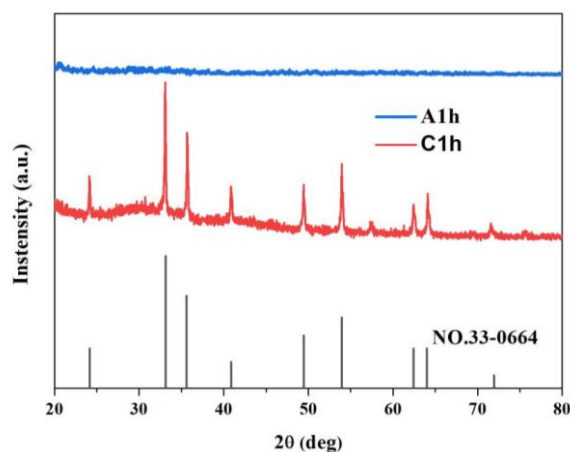


Figure 2. XRD patterns of the samples A1h and C1h.

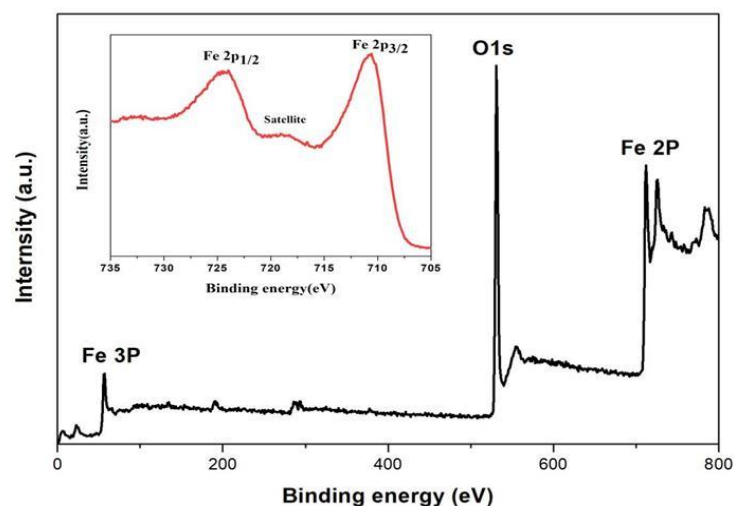


Figure 3. XPS survey and Fe 2p spectra (inset) of the amorphous sample (A1h).

There were two main effects of H<sup>+</sup> ions on the structure and morphology of the synthesized Fe<sub>2</sub>O<sub>3</sub>. On the one hand, H<sup>+</sup> ions corroded the crystal nuclei to form amorphous; on the other hand, H<sup>+</sup> ions corroded the surface of nanospheres into multiple staggered channels. In a high temperature and high pressure environment in the hydrothermal kettle, hematite nuclei formed due to the hydrolysis of the Fe<sup>3+</sup> ions in K<sub>3</sub>[Fe(CN)<sub>6</sub>] were easily etched by H<sup>+</sup> ions from NH<sub>4</sub>H<sub>2</sub>PO<sub>4</sub> [48]. The nuclei lost the periodicity of their original crystal structure. In other words, the nuclei became amorphous, as shown in Figure 1b, which then grew into amorphous nanoparticles. As the hydrothermal reaction continued, the amorphous nanoparticles converged into spheres to reduce the total surface energy. The surface of the spheres was smooth after reaction for 1 h, as shown in Figure 4a. Combined with the XRD pattern (Figure S1) and the electron diffraction (SAED)

pattern (Figure 4g) of the sample A1h, it could be determined that the sample A1h was amorphous. In addition, the high concentration of  $H^+$  ions in the solution continued to corrode  $Fe_2O_3$  nanospheres. A few holes appeared on the surface of nanoparticles after 3 h of hydrothermal reaction (Figure 4b). As the reaction time was increased to 6 h, the pores on the surface of the nanospheres continued to be corroded and grew to form irregular interconnected channels (Figure 4c). To reveal the surface characteristics of the nanospheres,  $N_2$  adsorption–desorption measurements were performed to obtain the BET surface area and the Barrett–Joyner–Halenda (BJH) pore size distribution profile, with the results shown in Figure S3. The sample A3h had a pore size distribution in the range of 2–10 nm, while the surface of the A6h sample had multiple small holes that were connected to form channels (30–60 nm). The results were consistent with the SEM observation. Representative TEM images of the samples reacted for different times are shown in Figure 4d–f, indicating the hollow structure of the  $Fe_2O_3$  nanospheres. With an increase in the hydrothermal treatment time, the wall thickness of the hollow nanospheres decreased. This observation can be understood according to the Ostwald ripening process, because the inner particles had a higher surface energy than the outer ones [48].

Electrochemical performances of the multi-channel surface modified amorphous  $Fe_2O_3$  nanospheres and the crystalline  $Fe_2O_3$  nanospheres were comparatively studied, in terms of cyclic voltammetry (CV) and galvanostatic charge/discharge curves. Figure 5 shows the CV curves of the two samples. CV curves of the crystalline  $\alpha$ - $Fe_2O_3$  nanospheres were similar to those previously reported in the literature [27,49–51]. Comparatively, there were three differences in the CV curve between the amorphous and the crystalline  $Fe_2O_3$  nanospheres. Firstly, the intensity of the reduction peak of the amorphous  $Fe_2O_3$  during the first two cycles was lower than that of the crystalline  $Fe_2O_3$ . This may be attributed to the long-range disorder of the amorphous state and its low reaction Gibbs free energy change ( $\Delta G$ ), i.e., lithium can be intercalated/deintercalated more easily in amorphous  $Fe_2O_3$ . The volume change of the amorphous electrode is a gradual process, different from the sudden change of the crystalline electrode, which is beneficial to the integrity and cycle stability of the electrode [16]. Secondly, the main cathode peak shifted by 0.05 V in the second cathodic scan and the magnitude of the peak shift was much smaller than that of the crystalline  $Fe_2O_3$ , which may have been caused by the better reversibility of the amorphous  $Fe_2O_3$  electrode. The peak near 1.2–1.4 V may be related to the formation of solid solution compounds, owing to the insertion of  $Li^+$  ions into the amorphous  $Fe_2O_3$  [52]. Finally, the first anodic scan of the amorphous electrode had two cathodic peaks at 1.47 V and 2.0 V, corresponding to the oxidation of  $Fe(0)$  to  $Fe^{2+}$  and further to  $Fe^{3+}$ , respectively.

Galvanostatic charge/discharge measurements were conducted at a current density of 100 mA/g in the voltage range of 0.005–3.0 V. As shown in Figure 6a,b, the first discharge specific capacity of the amorphous electrode (A6h) was 1187.3 mAh/g. The value of the crystalline electrode (C1h) was slightly higher (1305 mAh/g). The large irreversible capacity of the two samples in the first cycle was a common phenomenon, which is related to the decomposition of electrolyte and the formation of SEI layer [48]. The specific capacity of the crystalline sample decreased rapidly, while the value of the amorphous one was much stable. The values were 817 mAh/g, 815.5 mAh/g, 818.8 mAh/g, and 822.2 mAh/g in the four cycles. Figure 6c shows the cycle performances of the amorphous and the crystalline  $Fe_2O_3$  electrodes. Comparatively, the amorphous electrode had a higher cycle stability, with the specific capacity remaining at 875.2 mAh/g after 70 charge-discharge cycles. At the same time, the Coulombic efficiency was close to 100%. Moreover, the cycle specific capacity increased slightly, corresponding to a growth rate of 7.12%. The increase in the specific capacity of the amorphous electrode can be ascribed to the reversible formation of polymer gel-like film and the larger electrochemically active surface area of the  $Fe_2O_3$  shell [2,53,54]. With further cycling, the capacitive-like storage effect was strengthened, which is advantageous for high power applications [55]. In addition, the amorphous  $Fe_2O_3$  electrode (A6h) with multi-channel microstructure provided more active sites and space for

lithium intercalation, thus promoting the interfacial lithium storage of the active materials, which also contributed to the high specific capacity [11,56].

In order to further identify the difference in lithium-ion storage performance between the amorphous and the crystalline  $\text{Fe}_2\text{O}_3$  electrodes, rate performance tests were performed, with the results shown in Figure 6d. When the current density was increased from 100 to 2000 mA/g, the average discharge capacities of the amorphous electrode (A6h) and the crystalline one (C1h) decreased from 849.7 to 478.0 mAh/g and from 829.7 to 44.6 mAh/g, respectively. As the current density was restored to 100 mA/g, the specific capacity of the amorphous electrode quickly recovered to 783.3 mAh/g, which was much higher than that (544.2 mAh/g) of the crystalline electrode. The corresponding charge/discharge curves at different current densities are shown in Figure 6e,f, respectively. As the current density increased from 100 to 2000 mA/g, the discharge voltage plateau of the amorphous electrode (A6h) only slightly decreased, indicating that it had a relatively low polarization [57]. The outstanding rate performance is attributed to the well-distributed multi-channel structure, which offered a large electrode/electrolyte interface area and shortened the transport path of electrons and ions.

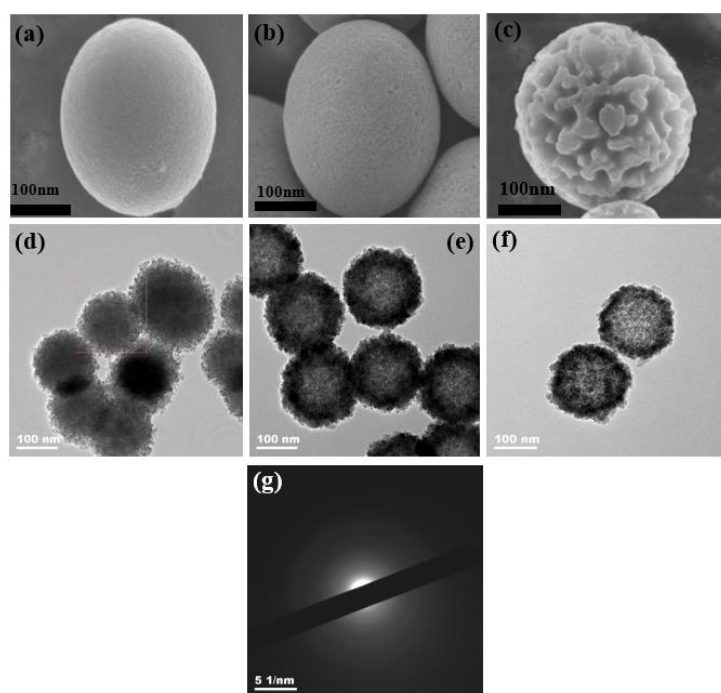


**Figure 4.** SEM images of the samples: (a) A1h, (b) A3h and (c) A6h. TEM images of the samples: (d) A1h, (e) A3h and (f) A6h. (g) SAED pattern of A1h.

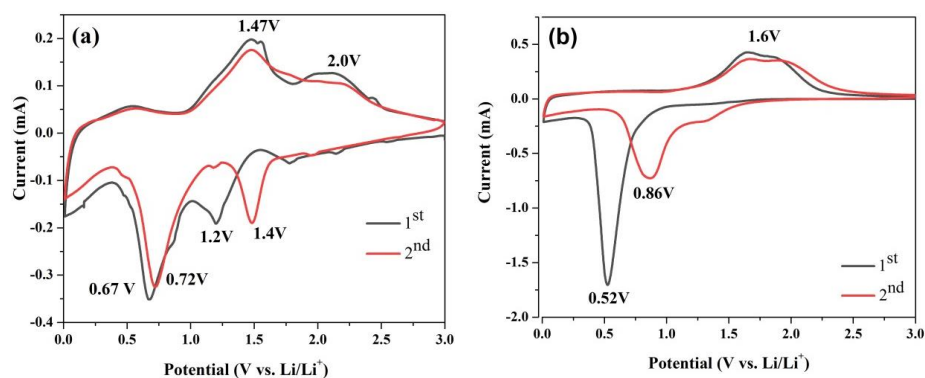


**Figure 5.** CV curves of the amorphous  $\text{Fe}_2\text{O}_3$  nanospheres A6h (a) and crystalline  $\alpha\text{-Fe}_2\text{O}_3$  nanospheres C1h (b).

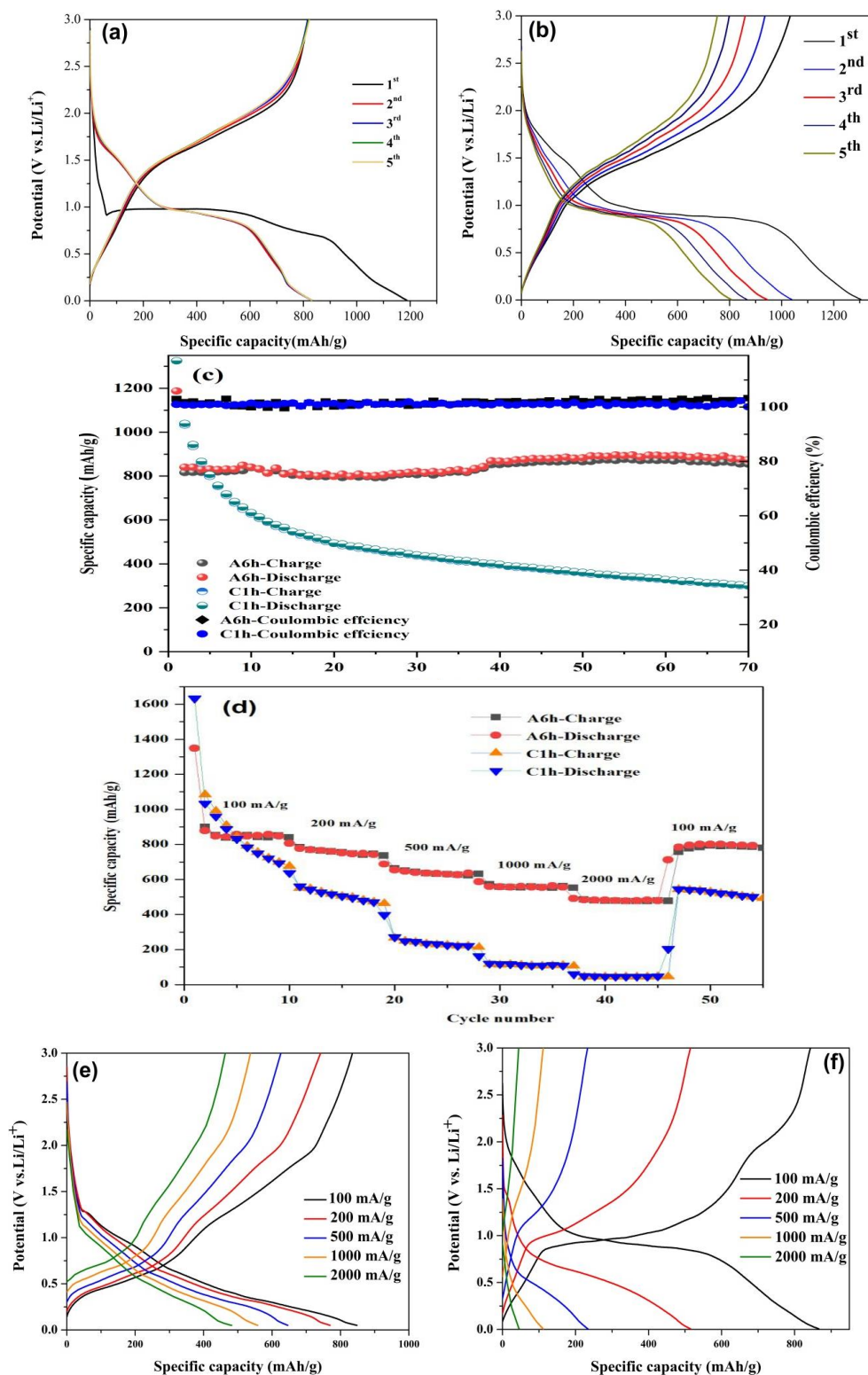


**Figure 6.** Discharge–charge voltage profiles of the amorphous and crystalline  $\text{Fe}_2\text{O}_3$  electrodes for the initial five cycles at a rate of 100 mA/g between 0.005 and 3.0 V: (a) A6h and (b) C1h. (c) Cycle performances of the A6h and C1h electrodes and their corresponding Coulombic efficiencies. (d) Rate performances of the A6h and C1h electrodes at different current rates. The fourth cycle charge/discharge profiles of amorphous and crystalline  $\text{Fe}_2\text{O}_3$  electrodes at different current densities: (e) A6h and (f) C1h.

Notably, the discharge/charge voltage curves of amorphous and crystalline Fe<sub>2</sub>O<sub>3</sub> electrodes during different cycles are shown in Figure S4. During the cycle, the discharge platforms of the amorphous Fe<sub>2</sub>O<sub>3</sub> electrodes were stable, indicating their low polarization and potential hysteresis [52]. The low potential hysteresis is linked with its faster kinetics and higher energy efficiency, which is an important factor for the practical applications [58]. In order to confirm this result and understand the ion diffusion kinetics, the galvanostatic intermittent titration (GITT) measurement was utilized to analyze the lithium ions transport kinetics of the electrode. Figure S5 shows the potential change of the sample as a function of time. The cells were repeatedly subject to a current pulse of 100 mA/g for 20 min and then relaxed for 240 min. The long relaxation time was used to full relaxation of lithium diffusion to reach equilibrium potential and minimize the self-discharge of Fe<sub>2</sub>O<sub>3</sub> during the test. The discharge/charge curves of the amorphous and crystalline electrodes showed similar trends. Current pulse step polarization curves of the amorphous and the crystalline Fe<sub>2</sub>O<sub>3</sub> electrodes at different potentials are shown in Figure 7a,b, respectively. According to the polarization curves, when the cells went to a higher voltage upon charging, it took more time to relax the pulse to reach a stable state (Figure 7(a2,b6)). Similarly, when the cells were discharged at a lower voltage, the pulse relaxation would be delayed (Figure 7(a3,b7)). These phenomena indicate that the lithium diffusion coefficient will change with the change of potential. Overpotential refers to the voltage difference between the equilibrium potential at the end of relaxation and that at the end of the current pulse ( $\approx \Delta E_\tau - \Delta E_s$ , ignoring IR drop) [59]. The overpotential during charging is greater than that during discharging. As clearly seen in Figure 7a,b, the voltage hysteresis of the amorphous electrode was significantly less pronounced than that of the crystalline electrode. The difference in polarization may be attributed to their difference in kinetics [60].

In order to better understand diffusion kinetics of Li<sup>+</sup>, galvanostatic intermittent titration (GITT) data were used to derive the diffusion coefficients ( $D_{Li^+}$ , cm<sup>2</sup>/s) of the Fe<sub>2</sub>O<sub>3</sub> electrodes, which can be estimated by using the Fick's law [55]:

$$D_{Li^+} = \frac{4}{\pi\tau} \left( \frac{m_b V_M}{M_b S} \right)^2 \left( \frac{\Delta E_s}{\Delta E_\tau} \right)^2 \quad (1)$$

where  $\tau$  is the constant current pulse time;  $m_b$ ,  $V_M$ ,  $M_b$  are the mass loading, molecular weight, molar volume of the active material, respectively,  $S$  is the effective area between the electrode and electrolyte,  $\Delta E_s$  and  $\Delta E_\tau$  represent the change of steady-state voltage and the total change of cell voltage during pulse subtracting the IR drop.  $D_{Li^+}$  values of the amorphous and the crystalline Fe<sub>2</sub>O<sub>3</sub> electrodes are shown in Figure 7c,d, respectively. It can be seen that the  $D_{Li^+}$  values in the two electrodes range from 10<sup>13</sup> to 10<sup>10</sup> cm<sup>2</sup>/s, in agreement with the reported data of  $\alpha$ -Fe<sub>2</sub>O<sub>3</sub> nanoparticles (10<sup>14</sup>–10<sup>11</sup> cm<sup>2</sup>/s) [61] and  $\alpha$ -Fe<sub>2</sub>O<sub>3</sub> electrode ( $9.96 \times 10^{13}$  cm<sup>2</sup>/s) [62]. It is worth noting that the amorphous electrode showed a higher  $D_{Li^+}$ , mainly because of the lack of grain boundaries, thus shortening the diffusion pathways and reducing the diffusion resistance.

Reaction kinetics of the amorphous and the crystalline Fe<sub>2</sub>O<sub>3</sub> electrodes were also evaluated by using electrochemical impedance spectroscopy (EIS). All Nyquist plots exhibited a recessed semicircle in the high-frequency region and a sloping line in the low-frequency region, which correspond to the charge transfer resistance and the diffusion impedance of Li<sup>+</sup>, respectively. As shown in Figure 8, the semicircular diameter of the amorphous Fe<sub>2</sub>O<sub>3</sub> electrode in the high frequency region is much smaller than that of the crystalline Fe<sub>2</sub>O<sub>3</sub> electrode. Therefore, amorphous Fe<sub>2</sub>O<sub>3</sub> greatly ensures a rapid charge transfer due to its amorphous nature, which facilitates faster lithiation/delithiation kinetics [29]. The EIS results are consistent with the cycle performances (Figure 6c) and the rate performances (Figure 6d).

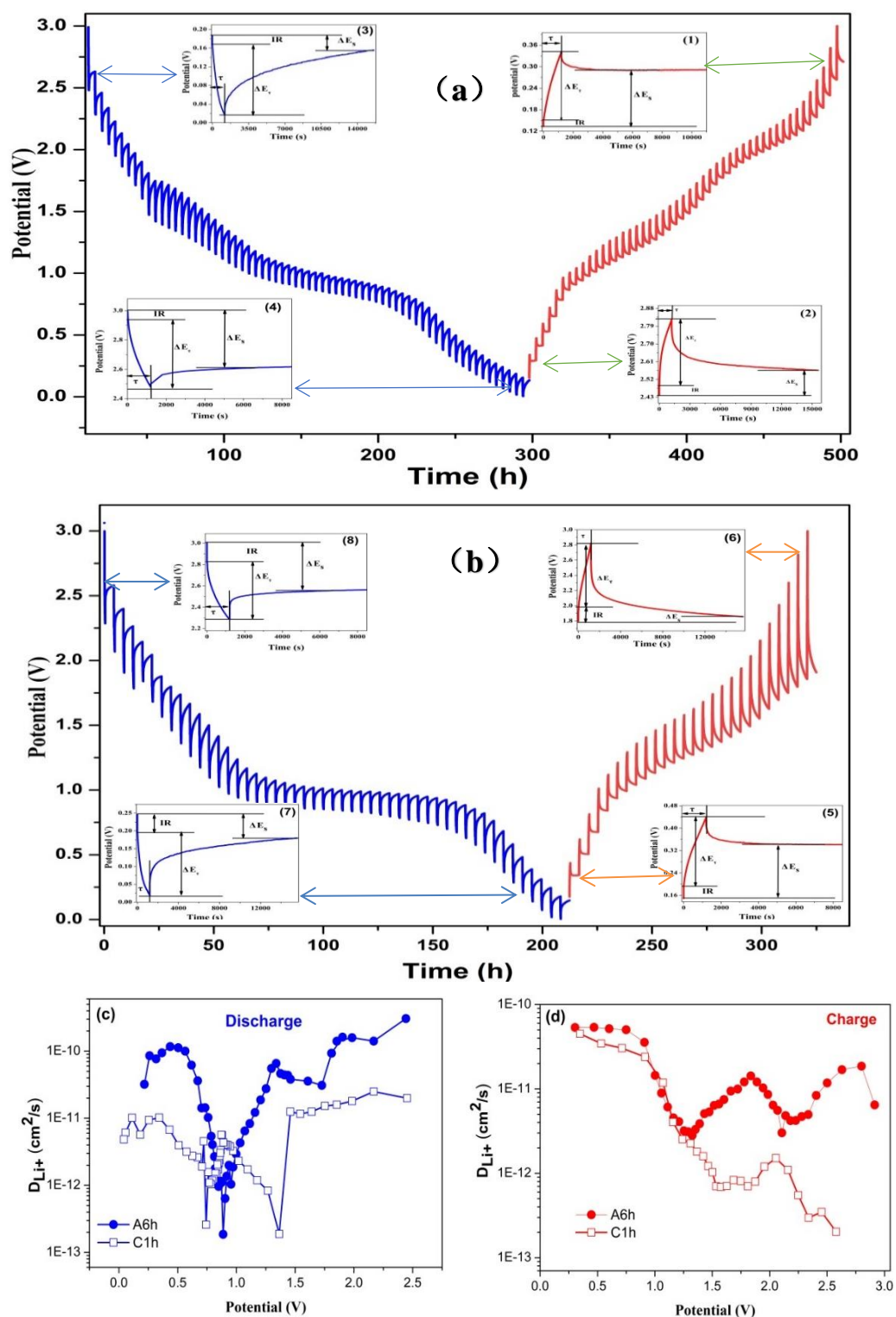


**Figure 7.** GITT profiles of the amorphous and crystalline  $\text{Fe}_2\text{O}_3$  electrodes: (a) A6h and (b) C1h. The insets show polarized curves for current pulse steps derived from the GITT data at different potentials in the discharge and charge processes. (c,d)  $\text{Li}^+$  diffusion coefficients of the electrodes during the discharge/charge process at various voltages derived from the GITT data: (a) A6h and (b) C1h.

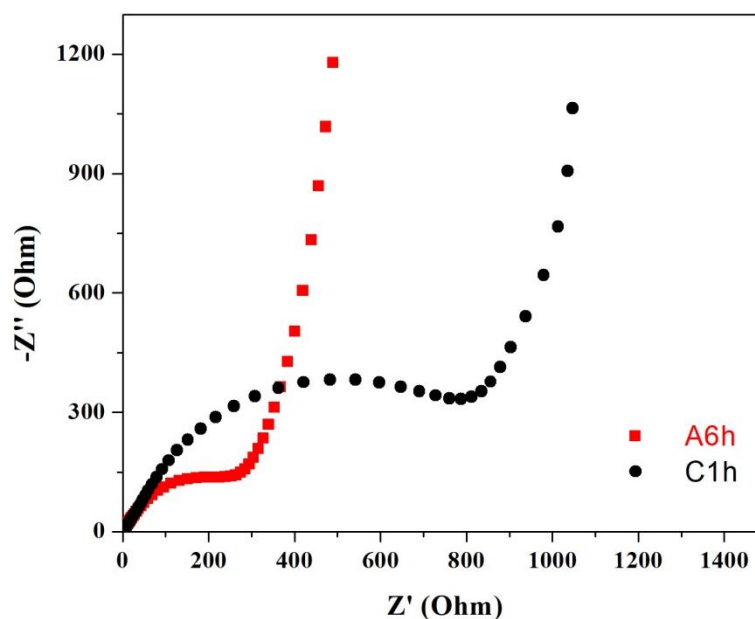


Figure 8. Nyquist plots of the amorphous and the crystalline  $\text{Fe}_2\text{O}_3$  electrodes.

#### 4. Conclusions

In summary, a simple, facile, and low-cost new strategy was demonstrated to design and fabricate multi-channel surface-modified amorphous  $\text{Fe}_2\text{O}_3$  nanospheres as anodes for Li-ion batteries in this study. When  $\text{NH}_4\text{H}_2\text{PO}_4$  existed in the precursor solution,  $\text{H}^+$  in the solution corroded the hydrolyzed hematite nuclei into amorphous  $\text{Fe}_2\text{O}_3$ . Based on the synergistic effect of ripening and hydrogen ion etching, multi-channel amorphous  $\text{Fe}_2\text{O}_3$  nanospheres could be formed by prolonging the hydrothermal treatment time. According to the test results of the crystalline state and microstructure of the material, it was found that surface structure of the amorphous  $\text{Fe}_2\text{O}_3$  nanospheres can be controlled by adjusting the reaction time. Owing to the isotropic nature and the lack of grain boundaries, the amorphous  $\text{Fe}_2\text{O}_3$  electrode facilitated high lithium-ion insertion and withstood high strains. The multi-channel surface-modified structure of the amorphous  $\text{Fe}_2\text{O}_3$  electrode not only ensured close contact between the internal active materials and the electrolyte, but also effectively alleviated the volume change during the intercalation/deintercalation of lithium ions. The multi-channel surface-modified amorphous  $\text{Fe}_2\text{O}_3$  nanospheres electrode exhibited excellent cycle stability (875.2 mAh/g after 70 cycles at 100 mA/g) and superior rate performance (56.3% capacity retention from 0.1 to 2.0 A/g) and narrow voltage hysteresis. The amorphous  $\text{Fe}_2\text{O}_3$  electrode exhibited faster electrochemical reaction kinetics, a higher  $\text{Li}^+$  diffusion coefficient, and a lower overpotential, as compared with its crystalline counterpart. The results in our present study can be used as a reference for the synthesis of amorphous transitional metal oxides (TMOs) as anodes of LIBs for practical applications.

**Supplementary Materials:** The following supporting information can be downloaded at: <https://www.mdpi.com/article/10.3390/en15165974/s1>, Figure S1. XRD patterns of the samples after hydrothermal treatment for different times (A1h, A3h, A6h); Figure S2. XPS spectrum (O 1s spectrum) of the amorphous  $\text{Fe}_2\text{O}_3$ ; Figure S3. Pore-size distributions of the amorphous  $\text{Fe}_2\text{O}_3$  samples: (a) A1h, (b) A3h and (c) A6h; Figure S4. Representative charge/discharge curves of the amorphous (a) and crystalline (b)  $\text{Fe}_2\text{O}_3$  electrodes; Figure S5. Close-up views of the GITT curves of the amorphous  $\text{Fe}_2\text{O}_3$  electrode.

**Author Contributions:** Data curation, S.Y. and W.Z.; Investigation, S.Y., W.Z., J.T., Q.W., T.C., X.H. and D.H.; Methodology, Y.W. and C.L.; Supervision, S.Y. and H.Z.; Writing—original draft, Y.W.; Writing—review and editing, S.Y. and H.Z. All authors have read and agreed to the published version of the manuscript.

**Funding:** This research was funded by the National Natural Science Foundation of China (No. 62041107, 61764007) and the Natural Science Foundation of Jiangxi Province (No. 20181BAB202005). This work was also funded by Jingdezhen Science and Technology Project (20212KJHZ002, 2021GYD009-03).

**Institutional Review Board Statement:** Not applicable.

**Informed Consent Statement:** Not applicable.

**Data Availability Statement:** Not applicable.

**Conflicts of Interest:** The authors declare no conflict of interest.

## References

1. Ryou, M.H.; Kim, J.; Lee, I.; Kim, S.; Jeong, Y.K.; Hong, S.; Ryu, J.H.; Kim, T.S.; Park, J.K.; Lee, H.; et al. Mussel-inspired adhesive binders for high-performance silicon nanoparticle anodes in lithium-ion batteries. *Adv. Mater.* **2013**, *25*, 1571–1576. [[CrossRef](#)] [[PubMed](#)]
2. Liu, L.; Huang, X.; Wei, Z.; Duan, X.; Zhong, B.; Xia, L.; Zhang, T.; Wang, H.; Jia, D.; Zhou, Y.; et al. Solvents adjusted pure phase  $\text{CoCO}_3$  as anodes for high cycle stability. *J. Adv. Ceram.* **2021**, *10*, 509–519. [[CrossRef](#)]
3. Zhao, Y.; Wang, J.; Ma, C.; Cao, L.; Shao, Z. A self-adhesive graphene nanoscroll/nanosheet paper with confined  $\text{Fe}_{1-x}\text{S}/\text{Fe}_3\text{O}_4$  hetero-nanoparticles for high-performance anode material of flexible Li-ion batteries. *Chem. Eng. J.* **2019**, *370*, 536–546. [[CrossRef](#)]
4. Wang, S.; Yang, Y.; Dong, Y.; Zhang, Z.; Tang, Z. Recent progress in Ti-based nanocomposite anodes for lithium ion batteries. *J. Adv. Ceram.* **2019**, *8*, 1–18. [[CrossRef](#)]
5. Pan, Q.; Zuo, P.; Mu, T.; Du, C.; Cheng, X.; Ma, Y.; Gao, Y.; Yin, G. Improved electrochemical performance of micro-sized SiO-based composite anode by prelithiation of stabilized lithium metal powder. *J. Power Sources* **2017**, *347*, 170–177. [[CrossRef](#)]
6. Wu, P.; Shi, B.; Tu, H.; Guo, C.; Liu, A.; Yan, G.; Yu, Z. Pomegranate-type Si/C anode with SiC taped, well-dispersed tiny Si particles for lithium-ion batteries. *J. Adv. Ceram.* **2021**, *10*, 1129–1139. [[CrossRef](#)]
7. Wu, M.; He, Y.; Wang, L.; Xia, Q.; Zhou, A. Synthesis and electrochemical properties of V<sub>2</sub>C MXene by etching in opened/closed environments. *J. Adv. Ceram.* **2020**, *9*, 749–758. [[CrossRef](#)]
8. Dong, Y.; Wang, B.; Zhao, K.; Yu, Y.; Wang, X.; Mai, L.; Jin, S. Air-Stable Porous  $\text{Fe}_2\text{N}$  Encapsulated in Carbon Microboxes with High Volumetric Lithium Storage Capacity and a Long Cycle Life. *Nano Lett.* **2017**, *17*, 5740–5746. [[CrossRef](#)]
9. Huang, H.; Gao, S.; Wu, A.-M.; Cheng, K.; Li, X.-N.; Gao, X.-X.; Zhao, J.-J.; Dong, X.-L.; Cao, G.-Z.  $\text{Fe}_3\text{N}$  constrained inside C nanocages as an anode for Li-ion batteries through post-synthesis nitridation. *Nano Energy* **2017**, *31*, 74–83. [[CrossRef](#)]
10. Li, H. In-Situ Grown Hierarchical  $\text{MoS}_2$  Nanoflakes on Three-Dimensional Carbon Fiber Papers as Free-Standing Anodes for Lithium-Ion Battery. *Int. J. Electrochem. Sci.* **2019**, *14*, 8662–8675. [[CrossRef](#)]
11. Zhao, Y.; Li, X.; Yan, B.; Xiong, D.; Li, D.; Lawes, S.; Sun, X. Recent Developments and Understanding of Novel Mixed Transition-Metal Oxides as Anodes in Lithium Ion Batteries. *Adv. Energy Mater.* **2016**, *6*, 1502175. [[CrossRef](#)]
12. Wang, S.; Tang, B.; Yang, W.; Wu, F.; Zhang, G.; Zhao, B.; He, X.; Yang, Y.; Jiang, J. The flower-like heterostructured  $\text{Fe}_2\text{O}_3/\text{MoS}_2$  coated by amorphous Si-Oxyhydroxides: An effective surface modification method for sulfide photocatalysts in photo-Fenton reaction. *J. Alloys Compd.* **2019**, *784*, 1099–1105. [[CrossRef](#)]
13. Yu, S.; Hong Ng, V.M.; Wang, F.; Xiao, Z.; Li, C.; Kong, L.B.; Que, W.; Zhou, K. Synthesis and application of iron-based nanomaterials as anodes of lithium-ion batteries and supercapacitors. *J. Mater. Chem. A* **2018**, *6*, 9332–9367. [[CrossRef](#)]
14. Ren, Z.; Yu, S.; Han, B.; Shao, Z.; Wang, Z. One-pot carbonization synthesis of  $\gamma\text{-Fe}_2\text{O}_3/\text{Fe}$ /carbon composite for high Li-storage and excellent stability. *Mater. Lett.* **2020**, *275*, 128066. [[CrossRef](#)]
15. Jin, Y.; Dang, L.; Zhang, H.; Song, C.; Lu, Q.; Gao, F. Synthesis of unit-cell-thick  $\alpha\text{-Fe}_2\text{O}_3$  nanosheets and their transformation to  $\gamma\text{-Fe}_2\text{O}_3$  nanosheets with enhanced LIB performances. *Chem. Eng. J.* **2017**, *326*, 292–297. [[CrossRef](#)]
16. Jiang, Y.; Zhang, D.; Li, Y.; Yuan, T.; Bahlawane, N.; Liang, C.; Sun, W.; Lu, Y.; Yan, M. Amorphous  $\text{Fe}_2\text{O}_3$  as a high-capacity, high-rate and long-life anode material for lithium ion batteries. *Nano Energy* **2014**, *4*, 23–30. [[CrossRef](#)]
17. Zhang, Z.; Han, Y.; Xu, J.; Ma, J.; Zhou, X.; Bao, J. Construction of Amorphous  $\text{FePO}_4$  Nanosheets with Enhanced Sodium Storage Properties. *ACS Appl. Energy Mater.* **2018**, *1*, 4395–4402. [[CrossRef](#)]
18. Zhu, X.; Jiang, X.; Chen, X.; Liu, X.; Xiao, L.; Cao, Y.  $\text{Fe}_2\text{O}_3$  amorphous nanoparticles/graphene composite as high-performance anode materials for lithium-ion batteries. *J. Alloys Compd.* **2017**, *711*, 15–21. [[CrossRef](#)]
19. Shi, L.; Li, Y.; Zeng, F.; Ran, S.; Dong, C.; Leu, S.-Y.; Boles, S.T.; Lam, K.H. In Situ growth of amorphous  $\text{Fe}_2\text{O}_3$  on 3D interconnected nitrogen-doped carbon nanofibers as high-performance anode materials for sodium-ion batteries. *Chem. Eng. J.* **2019**, *356*, 107–116. [[CrossRef](#)]
20. Wang, Z.; Wang, Z.; Liu, W.; Xiao, W.; Lou, X.W. Amorphous  $\text{CoSnO}_3@C$  nanoboxes with superior lithium storage capability. *Energy Environ. Sci.* **2013**, *6*, 87–91. [[CrossRef](#)]
21. Heitjans, P.; Tobschall, E.; Wilkening, M. Ion transport and diffusion in nanocrystalline and glassy ceramics. *Eur. Phys. J. Spec. Top.* **2008**, *161*, 97–108. [[CrossRef](#)]
22. Dash, U.; Sahoo, S.; Parashar, S.K.S.; Chaudhuri, P. Effect of  $\text{Li}^+$  ion mobility on the grain boundary conductivity of  $\text{Li}_2\text{TiO}_3$  nanoceramics. *J. Adv. Ceram.* **2014**, *3*, 98–108. [[CrossRef](#)]

23. Hüger, E.; Dörrer, L.; Rahn, J.; Panzner, T.; Stahn, J.; Lilienkamp, G.; Schmidt, H. Lithium Transport through Nanosized Amorphous Silicon Layers. *Nano Lett.* **2013**, *13*, 1237–1244. [[CrossRef](#)] [[PubMed](#)]
24. Li, X.; Meng, X.; Liu, J.; Geng, D.; Zhang, Y.; Banis, M.N.; Li, Y.; Yang, J.; Li, R.; Sun, X.; et al. Tin Oxide with Controlled Morphology and Crystallinity by Atomic Layer Deposition onto Graphene Nanosheets for Enhanced Lithium Storage. *Adv. Funct. Mater.* **2012**, *22*, 1647–1654. [[CrossRef](#)]
25. McDowell, M.T.; Lee, S.W.; Harris, J.T.; Korgel, B.A.; Wang, C.; Nix, W.D.; Cui, Y. In Situ TEM of Two-Phase Lithiation of Amorphous Silicon Nanospheres. *Nano Lett.* **2013**, *13*, 758–764. [[CrossRef](#)]
26. Xiong, H.; Slater, M.D.; Balasubramanian, M.; Johnson, C.S.; Rajh, T. Amorphous TiO<sub>2</sub> Nanotube Anode for Rechargeable Sodium Ion Batteries. *J. Phys. Chem. Lett.* **2011**, *2*, 2560–2565. [[CrossRef](#)]
27. Peng, P.; Zhao, Q.; Zhu, P.; Liu, W.; Yuan, Y.; Ding, R.; Gao, P.; Sun, X.; Liu, E. Amorphous Fe<sub>2</sub>O<sub>3</sub> film-coated mesoporous Fe<sub>2</sub>O<sub>3</sub> core-shell nanosphere prepared by quenching as a high-performance anode material for lithium-ion batteries. *J. Electroanal. Chem.* **2021**, *898*, 115633. [[CrossRef](#)]
28. Delmer, O.; Balaya, P.; Kienle, L.; Maier, J. Enhanced Potential of Amorphous Electrode Materials: Case Study of RuO<sub>2</sub>. *Adv. Mater.* **2008**, *20*, 501–505. [[CrossRef](#)]
29. Guo, J.; Liu, Q.; Wang, C.; Zachariah, M.R. Interdispersed Amorphous MnO<sub>x</sub>-Carbon Nanocomposites with Superior Electrochemical Performance as Lithium-Storage Material. *Adv. Funct. Mater.* **2012**, *22*, 803–811. [[CrossRef](#)]
30. Kumar, R.; Singh Rajesh, K.; Vaz Alfredo, R.; Savu, R.; Moshkalev Stanislav, A. Self-Assembled and One-Step Synthesis of Interconnected 3D Network of Fe<sub>3</sub>O<sub>4</sub>/Reduced Graphene Oxide Nanosheets Hybrid for High-Performance Supercapacitor Electrode. *ACS Appl. Mater. Interfaces* **2017**, *9*, 8880–8890. [[CrossRef](#)]
31. Qi, X.; Zhang, H.B.; Xu, J.; Wu, X.; Yang, D.; Qu, J.; Yu, Z.Z. Highly Efficient High-Pressure Homogenization Approach for Scalable Production of High-Quality Graphene Sheets and Sandwich-Structured  $\alpha$ -Fe<sub>2</sub>O<sub>3</sub>/Graphene Hybrids for High-Performance Lithium-Ion Batteries. *ACS Appl. Mater. Interfaces* **2017**, *9*, 11025–11034. [[CrossRef](#)] [[PubMed](#)]
32. Binitha, G.; Soumya, M.S.; Madhavan, A.A.; Praveen, P.; Balakrishnan, A.; Subramanian, K.R.V.; Reddy, M.V.; Nair, S.V.; Nair, A.S.; Sivakumar, N. Electrospun  $\alpha$ -Fe<sub>2</sub>O<sub>3</sub> nanostructures for supercapacitor applications. *J. Mater. Chem. A* **2013**, *1*, 11698. [[CrossRef](#)]
33. Park, Y.; Oh, M.; Park, J.S.; Baek, S.H.; Kim, M.; Kim, S.; Kim, J.H. Electrochemically deposited Fe<sub>2</sub>O<sub>3</sub> nanorods on carbon nanofibers for free-standing anodes of lithium-ion batteries. *Carbon* **2015**, *94*, 9–17. [[CrossRef](#)]
34. Gu, C.; Song, X.; Zhang, S.; Ryu, S.O.; Huang, J. Synthesis of hierarchical  $\alpha$ -Fe<sub>2</sub>O<sub>3</sub> nanotubes for high-performance lithium-ion batteries. *J. Alloys Compd.* **2017**, *714*, 6–12. [[CrossRef](#)]
35. Zhang, Y.; Yang, J.; Zhang, Y.; Li, C.; Huang, W.; Yan, Q.; Dong, X. Fe<sub>2</sub>O<sub>3</sub>/SnSSe Hexagonal Nanoplates as Lithium-Ion Batteries Anode. *ACS Appl. Mater. Interfaces* **2018**, *10*, 12722–12730. [[CrossRef](#)]
36. Zhang, L.; Wu, H.B.; Madhavi, S.; Hng, H.H.; Lou, X.W. Formation of Fe<sub>2</sub>O<sub>3</sub> microboxes with hierarchical shell structures from metal-organic frameworks and their lithium storage properties. *J. Am. Chem. Soc.* **2012**, *134*, 17388–17391. [[CrossRef](#)]
37. Cao, K.; Jiao, L.; Liu, H.; Liu, Y.; Wang, Y.; Guo, Z.; Yuan, H. 3D Hierarchical Porous  $\alpha$ -Fe<sub>2</sub>O<sub>3</sub> Nanosheets for High-Performance Lithium-Ion Batteries. *Adv. Energy Mater.* **2015**, *5*, 1401421. [[CrossRef](#)]
38. Cho, J.S.; Hong, Y.J.; Lee, J.H.; Kang, Y.C. Design and synthesis of micron-sized spherical aggregates composed of hollow Fe<sub>2</sub>O<sub>3</sub> nanospheres for use in lithium-ion batteries. *Nanoscale* **2015**, *7*, 8361–8367. [[CrossRef](#)]
39. Han, Y.; Wang, Y.; Li, L.; Wang, Y.; Jiao, L.; Yuan, H.; Liu, S. Preparation and electrochemical performance of flower-like hematite for lithium-ion batteries. *Electrochim. Acta* **2011**, *56*, 3175–3181. [[CrossRef](#)]
40. Ma, X.H.; Feng, X.Y.; Song, C.; Zou, B.K.; Ding, C.X.; Yu, Y.; Chen, C.H. Facile synthesis of flower-like and yarn-like  $\alpha$ -Fe<sub>2</sub>O<sub>3</sub> spherical clusters as anode materials for lithium-ion batteries. *Electrochim. Acta* **2013**, *93*, 131–136. [[CrossRef](#)]
41. Zhou, Y.; Hao, W.; Zhao, X.; Zhou, J.; Yu, H.; Lin, B.; Liu, Z.; Pennycook, S.J.; Li, S.; Fan, H.J. Electronegativity Induced Charge Balancing to Boost Stability and Activity of Amorphous Electrocatalyst. *Adv. Mater.* **2021**, *34*, e2100537. [[CrossRef](#)]
42. Hu, X.; Yu, J.C.; Gong, J. Fast Production of Self-Assembled Hierarchical  $\alpha$ -Fe<sub>2</sub>O<sub>3</sub> Nanoarchitectures. *J. Phys. Chem. C* **2007**, *111*, 11180–11185. [[CrossRef](#)]
43. Yan, Y.; Tang, H.; Wu, F.; Wang, R.; Pan, M. One-Step Self-Assembly Synthesis  $\alpha$ -Fe<sub>2</sub>O<sub>3</sub> with Carbon-Coated Nanoparticles for Stabilized and Enhanced Supercapacitors Electrode. *Energies* **2017**, *10*, 1296. [[CrossRef](#)]
44. Park, G.D.; Park, S.-K.; Kang, Y.C. Superior Electrochemical Properties of Composite Microspheres Consisting of Hollow Fe<sub>2</sub>O<sub>3</sub> Nanospheres and Graphitic Carbon. *ACS Sustain. Chem. Eng.* **2018**, *6*, 11759–11767. [[CrossRef](#)]
45. Park, G.D.; Hong, J.H.; Jung, D.S.; Lee, J.-H.; Kang, Y.C. Unique structured microspheres with multishells comprising graphitic carbon-coated Fe<sub>3</sub>O<sub>4</sub> hollow nanopowders as anode materials for high-performance Li-ion batteries. *J. Mater. Chem. A* **2019**, *7*, 15766–15773. [[CrossRef](#)]
46. Hsu, L.-C.; Li, Y.-Y.; Lo, C.-G.; Huang, C.-W.; Chern, G. Thermal growth and magnetic characterization of  $\alpha$ -Fe<sub>2</sub>O<sub>3</sub> nanowires. *J. Phys. D Appl. Phys.* **2008**, *41*, 185003. [[CrossRef](#)]
47. Sun, S.; Zhai, T.; Liang, C.; Savilov, S.V.; Xia, H. Boosted crystalline/amorphous Fe<sub>2</sub>O<sub>3</sub>- $\delta$  core/shell heterostructure for flexible solid-state pseudocapacitors in large scale. *Nano Energy* **2018**, *45*, 390–397. [[CrossRef](#)]
48. Sun, P.; Wang, B.; Zhao, L.; Gao, H.; Wang, T.; Yang, X.; Liu, C.; Lu, G. Enhanced gas sensing by amorphous double-shell Fe<sub>2</sub>O<sub>3</sub> hollow nanospheres functionalized with PdO nanoparticles. *Sens. Actuators B Chem.* **2017**, *252*, 322–329. [[CrossRef](#)]

49. Zhu, J.; Yin, Z.; Yang, D.; Sun, T.; Yu, H.; Hoster, H.E.; Hng, H.H.; Zhang, H.; Yan, Q. Hierarchical hollow spheres composed of ultrathin Fe<sub>2</sub>O<sub>3</sub> nanosheets for lithium storage and photocatalytic water oxidation. *Energy Environ. Sci.* **2013**, *6*, 987–993. [[CrossRef](#)]
50. Lv, X.; Deng, J.; Wang, J.; Zhong, J.; Sun, X. Carbon-coated  $\alpha$ -Fe<sub>2</sub>O<sub>3</sub> nanostructures for efficient anode of Li-ion battery. *J. Mater. Chem. A* **2015**, *3*, 5183–5188. [[CrossRef](#)]
51. Wang, B.; Chen, J.S.; Wu, H.B.; Wang, Z.; Lou, X.W. Quasiemulsion-templated formation of  $\alpha$ -Fe<sub>2</sub>O<sub>3</sub> hollow spheres with enhanced lithium storage properties. *J. Am. Chem. Soc.* **2011**, *133*, 17146–17148. [[CrossRef](#)]
52. Huang, Y.; Lin, Z.; Zheng, M.; Wang, T.; Yang, J.; Yuan, F.; Lu, X.; Liu, L.; Sun, D. Amorphous Fe<sub>2</sub>O<sub>3</sub> nanoshells coated on carbonized bacterial cellulose nanofibers as a flexible anode for high-performance lithium ion batteries. *J. Power Sources* **2016**, *307*, 649–656. [[CrossRef](#)]
53. Jiang, X.; Yang, X.; Zhu, Y.; Yao, Y.; Zhao, P.; Li, C. Graphene/carbon-coated Fe<sub>3</sub>O<sub>4</sub> nanoparticle hybrids for enhanced lithium storage. *J. Mater. Chem. A* **2015**, *3*, 2361–2369. [[CrossRef](#)]
54. Wang, X.; Wu, X.-L.; Guo, Y.-G.; Zhong, Y.; Cao, X.; Ma, Y.; Yao, J. Synthesis and Lithium Storage Properties of Co<sub>3</sub>O<sub>4</sub> Nanosheet-Assembled Multishelled Hollow Spheres. *Adv. Funct. Mater.* **2010**, *20*, 1680–1686. [[CrossRef](#)]
55. Sun, B.; Lou, S.; Qian, Z.; Zuo, P.; Du, C.; Ma, Y.; Huo, H.; Xie, J.; Wang, J.; Yin, G. Pseudocapacitive Li<sup>+</sup> storage boosts ultrahigh rate performance of structure-tailored CoFe<sub>2</sub>O<sub>4</sub>@Fe<sub>2</sub>O<sub>3</sub> hollow spheres triggered by engineered surface and near-surface reactions. *Nano Energy* **2019**, *66*, 104179. [[CrossRef](#)]
56. Jin, R.; Ma, Y.; Sun, Y.; Li, H.; Wang, Q.; Chen, G. Manganese Cobalt Oxide (MnCo<sub>2</sub>O<sub>4</sub>) Hollow Spheres as High Capacity Anode Materials for Lithium-Ion Batteries. *Energy Technol.* **2017**, *5*, 293–299. [[CrossRef](#)]
57. Xin, J.; Jia-jia, C.; Jian-hui, X.; Yi-ning, S.; You-zuo, F.; Min-sen, Z.; Quan-feng, D. Fe<sub>2</sub>O<sub>3</sub> xerogel used as the anode material for lithium ion batteries with excellent electrochemical performance. *Chem. Commun.* **2012**, *48*, 7410–7412. [[CrossRef](#)]
58. Etacheri, V.; Marom, R.; Elazari, R.; Salitra, G.; Aurbach, D. Challenges in the development of advanced Li-ion batteries: A review. *Energy Environ. Sci.* **2011**, *4*, 3243–3262. [[CrossRef](#)]
59. Zhu, Y.; Wang, C. Strain accommodation and potential hysteresis of LiFePO<sub>4</sub> cathodes during lithium ion insertion/extraction. *J. Power Sources* **2011**, *196*, 1442–1448. [[CrossRef](#)]
60. Li, Y.; Ji, J.; Yao, J.; Zhang, Y.; Huang, B.; Cao, G. Sodium ion storage performance and mechanism in orthorhombic V<sub>2</sub>O<sub>5</sub> single-crystalline nanowires. *Sci. China Mater.* **2020**, *64*, 557–570. [[CrossRef](#)]
61. Yao, J.; Yang, Y.; Li, Y.; Jiang, J.; Xiao, S.; Yang, J. Interconnected  $\alpha$ -Fe<sub>2</sub>O<sub>3</sub> nanoparticles prepared from leaching liquor of tin ore tailings as anode materials for lithium-ion batteries. *J. Alloys Compd.* **2021**, *855*, 157288. [[CrossRef](#)]
62. Wu, C.; Xu, Y.; Ao, L.; Jiang, K.; Shang, L.; Li, Y.; Hu, Z.; Chu, J. Robust three-dimensional porous rGO aerogel anchored with ultra-fine  $\alpha$ -Fe<sub>2</sub>O<sub>3</sub> nanoparticles exhibit dominated pseudocapacitance behavior for superior lithium storage. *J. Alloys Compd.* **2020**, *816*, 152627. [[CrossRef](#)]